



OPEN Unveiling the role of dual grading in device optimization of HTL-free $\text{Sb}_2(\text{S}, \text{Se})_3$ solar cells

Basma A. A. Osman¹, Ahmed Shaker^{2✉}, Ibrahim S. Ahmed¹ & Tarek M. Abdolkader¹

Antimony Seleno-sulfide, $\text{Sb}_2(\text{S}, \text{Se})_3$, is considered an extremely promising absorber for optoelectronic applications regarding its minor toxicity, phase stability, earth-abundance besides its decent absorption capabilities. Moreover, it possesses tunable bandgaps which can be adjusted from 1.1 to 1.7 eV by varying the Se/S ratio in $\text{Sb}_2(\text{S}, \text{Se})_3$ alloy films, making it an attractive candidate for efficient solar cells. This study proposes novel designs for hole-transporting layer (HTL)-free $\text{Sb}_2(\text{S}, \text{Se})_3$ solar cells that enhance photo-generated carrier collection, thereby improving power conversion efficiency (PCE). Utilizing SCAPS-1D solar cell simulator, we first validate the device model by calibrating an experimental cell with the FTO/CdS/ $\text{Sb}_2(\text{S}, \text{Se})_3$ /Au configuration. The primary objective is to optimize HTL-free $\text{Sb}_2(\text{S}, \text{Se})_3$ solar cells using dual grading techniques in the electron-transport layer (ETL) and within the absorber. Our analysis reveals that the band offsets at both the ETL/absorber and ETL/front contact interfaces play competing roles in determining cell performance. To optimize these offsets, we replace the traditional CdS ETL with the tunable $\text{Cd}_{1-x}\text{Zn}_x\text{S}$ and gradually adjust the Zn fraction at both interfaces. We also conduct a comparative study of various bandgap grading (BGG) profiles (linear, logarithmic, and parabolic). A doping grading technique is also applied to the absorber to enhance charge carrier extraction. The simulation results indicate that dual grading techniques in the ETL and absorber, combined with optimized absorber thickness, can significantly improve device performance, yielding a simulated PCE of 21.15%. These findings provide valuable insights into the design and optimization of HTL-free $\text{Sb}_2(\text{S}, \text{Se})_3$ solar cells.

Keywords $\text{Sb}_2(\text{S}, \text{Se})_3$, Bandgap grading, Doping grading, CBO, CdZnS, HTL free

In recent years, the transition to renewable energy has significantly enhanced productivity and quality of life, serving as a cornerstone for economic and social development¹. One of the most prominent types of renewable energy sources that is currently advancing quickly to keep up with the growing global energy issues is solar energy². To improve power conversion efficiency (PCE), several solar cell (SC) technologies have been studied³. Despite advancements in technologies such as microstructures and nanowires aimed at enhancing PCE and reducing costs⁴, the efficiencies achieved with these approaches still fall short compared to those of crystalline silicon (c-Si) solar cells, known for their outstanding PCE and stability in various applications. However, thin-film solar cells are becoming a perfect substitute for Si-based solar cells thanks to their affordable prices, high efficiency, and enhanced device flexibility^{5,6}. CdTe and CuInGaSe₂ are distinguished examples of photovoltaic (PV) thin films, which are commonly utilized in flexible devices and for constructing integrated PV systems⁷. Nevertheless, their use is somewhat limited by the rarity of In, Te, and Ga as well as the toxicity of Cd. Therefore, research is necessary to find nontoxic, Earth-abundant PV materials such as Sb_2S_3 ⁸, Sb_2Se_3 ⁹, $\text{Sb}_2(\text{S}, \text{Se})_3$ ⁹, CuSbSe₂¹⁰, CuSbS₂¹¹, and other candidates.

The family of Antimony Chalcogenide binary compounds Sb_2Se_3 , Sb_2S_3 and $\text{Sb}_2(\text{S}, \text{Se})_3$ thin film cells has witnessed substantial progress in the last few years. An inorganic Antimony Selenide (V-VI binary compound), Sb_2Se_3 , is a very suitable SC light absorber due to its attractive optoelectronic properties such as superior electrical conductivity, absorption coefficients larger than 10^5 cm^{-1} , nearly 60 ns carrier lifetime, and bandgap (1.03–1.17 eV)¹² which is proper and close to the optimum value of Shockley-Queisser, aside from its rare toxicity, and appropriate price¹³. Advantages also include its single orthorhombic structure and 1D crystalline structure¹⁴. Additionally, antimony sulfide, Sb_2S_3 , has impressive properties for solar cells. It is one of the most promising light-absorbers for the fact that Sb_2S_3 is low-cost, environmentally friendly, and abundant on earth. Besides, it

¹Department of Basic Engineering Sciences, Benha Faculty of Engineering, Benha University, Benha, Egypt.

²Department of Engineering Physics and Mathematics, Faculty of Engineering, Ain Shams University, Cairo, Egypt.

✉email: ahmed.shaker@eng.asu.edu.eg

has an acceptable bandgap of nearly 1.7 eV, a superior absorption coefficient of approximately $2 \times 10^5 \text{ cm}^{-1}$, and sufficient air-stability⁸. The same crystal structure of Sb_2S_3 and Sb_2Se_3 permits tuning the bandgap of $\text{Sb}_2(\text{S}, \text{Se})_3$ from about 1.1 eV to 1.7 eV by modifying the Se/S atomic ratio¹⁵. Adjusting the Se/S atomic ratio results in a more acceptable absorber bandgap for light harvesting, in addition to a compact morphology, larger grains and favorable crystal orientation¹⁶. The p-type $\text{Sb}_2(\text{S}, \text{Se})_3$ semiconductor features a tunable absorption cutoff edge (730–1050 nm)¹⁷. Recently, the PCE of $\text{Sb}_2(\text{S}, \text{Se})_3$ -based thin films SCs reached above 10% efficiency¹⁶.

Choosing a suitable ETL for $\text{Sb}_2(\text{S}, \text{Se})_3$ -based SCs is extremely important to dismiss absorption losses and improve interface performance between absorber and ETL. The stability and large electron mobility of CdS make it an ideal ETL material for $\text{Sb}_2(\text{S}, \text{Se})_3$ SCs⁹. Conversely, it confronts two serious issues: (1) absorption at long wavelengths owing to the relatively small bandgap (2.42 eV)^{8,18} and (2) the undesired recombination at the interface between CdS/ $\text{Sb}_2(\text{S}, \text{Se})_3$, due to the unoptimized band alignment between them. As a result, it was found that lowering the thickness or substituting the CdS layer with a larger gap layer such as SnO_2 , TiO_2 , ZnO, or ZnMgO are possible solutions¹⁹. In addition, the fabrication of double buffer layers is another possible solution; however, it seems to be extremely challenging. One suitable strategy for increasing the CdS bandgap to permit absorbing more photons in the absorber layer is to add more dopant atoms or replace Cd or S with alternative atoms. Ternary $\text{Cd}_{1-x}\text{Zn}_x\text{S}$ ($0 \leq x \leq 1$) compound is an acceptable alternative to CdS as an ETL as it modifies electron affinity and energy bandgap¹⁸. The bandgap may be modified by adjusting the Zn concentration and the band alignment between buffer/absorber¹⁸. The role of $\text{Cd}_{1-x}\text{Zn}_x\text{S}$ as an ETL in fabricated cells increased efficiency from 5.08 to 6.71%, as reported previously²⁰. In a simulation study, the authors simulated an Au/ $\text{Sb}_2(\text{S}, \text{Se})_3$ /CdS/ITO structure. The optimized cell achieved a simulated 14.86% PCE by employing $\text{Cd}_{0.44}\text{Zn}_{0.56}\text{S}$ as an ETL to tune the conduction band offset (CBO) between the absorber and the ETL, as well as various other factors¹⁸.

Numerous methodologies, both experimental and simulation based, were applied to boost the PCE of $\text{Sb}_2(\text{S}, \text{Se})_3$ -based SCs. Kanghua Li et al., investigated a new approach to optimize the ITO/CdS/ $\text{Sb}_2(\text{S}, \text{Se})_3$ /Au cell arrangement. They used vapor transport deposition (VTD) technology to design an $\text{Sb}_2(\text{S}, \text{Se})_3$ cell with V-shaped bandgap energy. They obtained a PCE of 7.27% after optimization¹⁷. In 2020, a PCE of 10.0% was reported by studying a novel Se/(S+Se) atomic ratio of 29% in FTO/CdS/ $\text{Sb}_2(\text{S}, \text{Se})_3$ SCs to get an acceptable bandgap of $\text{Sb}_2(\text{S}, \text{Se})_3$ ¹⁶. In 2021, researchers introduced a theoretical triple-junction $\text{Sb}_2\text{S}_3/\text{Sb}_{2(0.7\text{Se}_{0.3})_3}/\text{Sb}_2\text{Se}_3$ SC utilizing several band alignment strategies. Raising the concentration of Se in the $\text{Sb}_2(\text{S}_{1-x}\text{Se}_x)_3$ -based solar cell resulted in a theoretical efficiency of 33%²¹. Moreover, it was discovered that an $\text{Sb}_2(\text{S}, \text{Se})_3$ SC with a Sb_2S_3 mass ratio of 0.25% between Sb_2S_3 and the overall powder had the best crystallinity. This concept has been used in ITO/CdS/ $\text{Sb}_2(\text{S}, \text{Se})_3$ /Au SCs, yielding 7.31% PCE¹⁷. Furthermore, Junwei Chen et al. found that applying TA- $\text{Sb}_2(\text{S}, \text{Se})_3$ in a planar heterojunction SC yielded a PCE of 9.28% and a V_{oc} of 0.7 V²². To manage the chemical interaction of Sb material with Se and S in $\text{Sb}_2(\text{S}, \text{Se})_3$, the hydrothermal temperature must be adjusted. This process resulted in a device possessing the highest PCE of 10.55% among $\text{Sb}_2(\text{S}, \text{Se})_3$ -based SCs until now²³. In 2024, Lei Zhang et al. used alkali halide (CsI) as a precursor in hydrothermal processes to enhance the performance of antimony selenosulfide SCs. This causes a rise in PCE to 10.05%²⁴. In 2023, Yue Deng et al. developed a two-step hydrothermal deposition process for making $\text{Sb}_2\text{S}_3/\text{Sb}_2(\text{S}, \text{Se})_3$ films with big grains and smooth surfaces. Applying these films in SnO_2 /CdS/ $\text{Sb}_2\text{S}_3/\text{Sb}_2(\text{S}, \text{Se})_3$ /carbon SCs yielded a PCE of 2.76%. After that, they used P_3HT as HTL and got a PCE of 4.15%²⁵. Wangchao Chen et al. constructed two HTLs (free dopant materials) named F-BDT and T-BDT. They realized that the cell F-BDT/ $\text{Sb}_2(\text{S}, \text{Se})_3$ achieved 9.13% efficiency²⁶.

Although SCs utilizing organic HTL materials, such as P_3HT ₅ and Spiro-OMeTAD, achieved a high PCE²⁷, these HTL materials have undesirable features, such as low long-term stability and high fabrication cost²⁷. To deal with these issues, HTL-free SCs have been introduced to the PV community²⁸. These cells would lower interface defects between HTL and absorber as well as fabrication expenses^{2,27}. For instance, HTL-free $\text{Sb}_2(\text{S}, \text{Se})_3$ SC structure was manufactured by VTD process with $E_g = 1.33 \text{ eV}$, achieving a PCE of 7.03%²⁸. To further increase PCE in the free HTL design, the CBO between the ETL and the absorber needs to be aligned. This alignment may be achieved by employing an adjustable bandgap ETL material such as $\text{Cd}_{1-x}\text{Zn}_x\text{S}$ ²⁹.

One of the most critical factors in an n-i-p heterojunction is the precise band alignment, not only between the absorber layer and the ETL, but also between the ETL and the front contact. Proper band alignment at both interfaces is essential to minimize energy losses, enhance carrier extraction, and prevent recombination. Through the adjustment of bands, a smoother transportation of electrons from the absorber through the ETL to the front contact (FC) can be obtained, resulting in boosting the PCE of the SC. Thus, in this paper, we introduce a design of a single junction HTL-free $\text{Sb}_2(\text{S}, \text{Se})_3$ SC. The aim is to obtain a proper band alignment through the whole structure, not just at the carrier-transporting layer/absorber interface as usually encountered. This is performed by using a grading technique in the ETL, including linear, logarithmic, and parabolic BGG profiles along with doping grading within the absorber layer. The proposed structure is designed without a hole-transport layer, aiming to reduce interface and stability issues commonly associated with organic HTLs. Validation of the suggested model is needed to verify that the physical parameters are similar to the technological parameters. Accordingly, a calibration step is performed to validate the simulation reliability by benchmarking a simulated cell model against a similar fabricated cell whose structure is ITO/CdS/ $\text{Sb}_2(\text{S}, \text{Se})_3$ /Au. Next, we replace the CdS ETL with $\text{Cd}_{1-x}\text{Zn}_x\text{S}$ and vary the composition x of Zn to obtain graded ETL concentrations. These different compositions enable us to grade the bandgap from absorber to the FC and get the best alignment between them. Consequently, we choose the best absorber doping concentration (N_a) and compare it with grading the acceptor doping concentration of the absorber. Finally, we optimize this cell by simultaneously selecting the optimal thickness (t_{abs}) and the bulk defect density (N_p). All this work is performed by the numerical simulator SCAPS-1D software under AM1.5G irradiation.

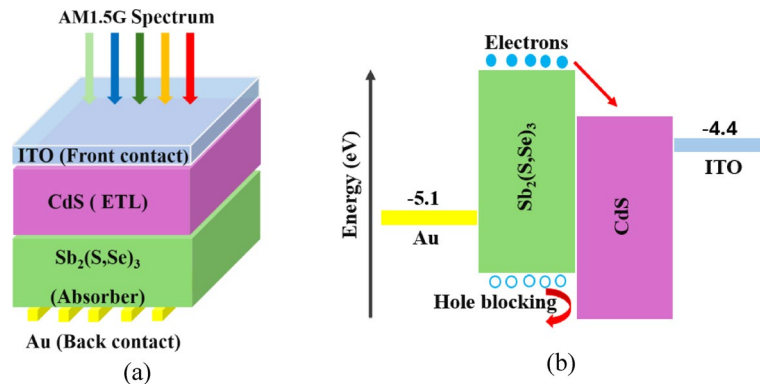


Fig. 1. $\text{Sb}_2(\text{S}, \text{Se})_3$ cell structure: (a) critical films ITO/CdS/ $\text{Sb}_2(\text{S}, \text{Se})_3$ /Au, (b) CB and VB profile and flow of electrons and holes in cell.

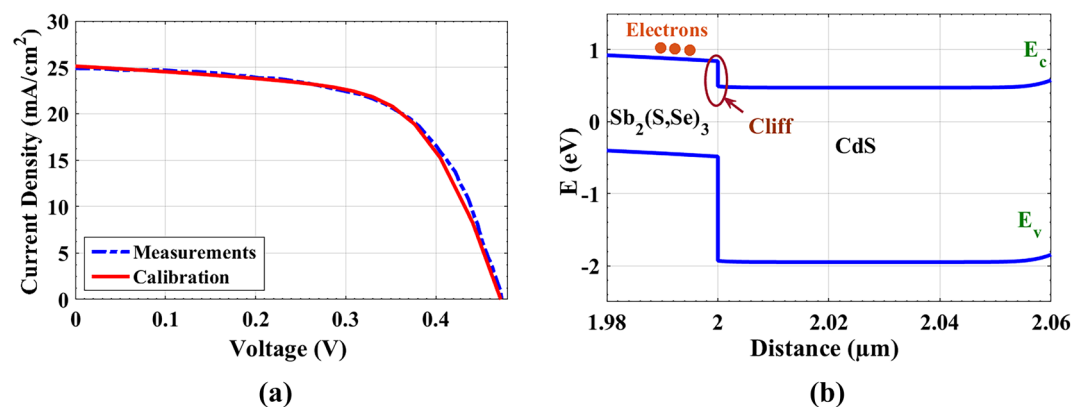


Fig. 2. (a) Comparison of current density versus voltage curves for both experimental and calibrated $\text{Sb}_2(\text{S}, \text{Se})_3$ -based SCs without HTL, (b) Energy band profile of $\text{Sb}_2(\text{S}, \text{Se})_3$ and CdS at illumination and at J_{sc} conditions.

Simulation method and main device structure

In this section, we introduce the HTL-free $\text{Sb}_2(\text{S}, \text{Se})_3$ SC design, based on the configuration: ITO/CdS/ $\text{Sb}_2(\text{S}, \text{Se})_3$ /Au. In doing our simulations, SCAPS-1D has been chosen as a device simulator platform³⁰. Based on collected data from the literature, a validation step has been conducted through the calibration of simulated SC versus experiments. Some parameters are engineered to fit experimental data.

SCAPS-1D

In this work, we used one dimensional numerical simulator SCAPS which has been progressed in Belgium (Gent university)³¹. Notably, SCAPS became a versatile and generally accepted tool that proved to be reliable, giving accurate simulation results which agree with the experimental investigations³¹. Poisson equation and continuity equations for hole and electron are the main equations used in SCAPS-1D. Auger and Shockley-Read-Hall (SRH) recombination models are implemented in it which are very essential for SC evaluation, especially in solar cells having high doping regions and high defect densities¹⁸. To get high performance and accurate simulation from it, other different factors also are considered like irradiance, temperature, and electrical bias conditions³². Current density–voltage (J–V), capacitance–voltage and -frequency (C–V, C–f) characteristics as well as External Quantum Efficiency (EQE) can be extracted from simulation helping for further optimization³².

Device structure and its parameters

The configuration and the energy bandgap diagram (EBD) of the device used are explained in Fig. 1. The solar cell contains a transparent front contact (ITO), ETL (CdS), absorber ($\text{Sb}_2(\text{S}, \text{Se})_3$) and back electrode (Au), as shown in Fig. 1(a). The flow of free carriers (electrons and holes) according to the values of affinity and CBO from absorber to the ETL and rear contact is shown in Fig. 1(b). The conduction and valence band (CB & VB) are also shown. All the basic physical and technological factors of CdS and $\text{Sb}_2(\text{S}, \text{Se})_3$ are illustrated in Table 1, which are acquired from previous experimental and simulation research^{21,28}. The work function of the rear electrode is 5.1 eV, while that of the FC is 4.4 eV, as shown in Fig. 1(b). The introduced baseline HTL-free $\text{Sb}_2(\text{S}, \text{Se})_3$ SC was fabricated according to X. Hu. and his team³³. The CdS layer, serving as an ETL, was deposited on

Material Parameters	CdS	CdZnS	Sb ₂ (S, Se) ₃
Thickness (nm)	60	60	2000
Energy gap (eV)	2.42	2.42–3.54	1.325
Affinity (eV)	4.305	4.305–3.185	3.955
Relative permittivity	9	9	15
Hole/Electron mobility (cm ² /V.s)	25/100	25/100	3/8
VB/CB effective DOS (cm ⁻³)	1.8 × 10 ¹⁹ /2.2 × 10 ¹⁸	1.8 × 10 ¹⁹ /2.2 × 10 ¹⁸	1.8 × 10 ¹⁸ /1 × 10 ¹⁸
Acceptor level (cm ⁻³)	--	--	3.6 × 10 ¹⁶
Donor level (cm ⁻³)	2.9 × 10 ¹⁸	2.9 × 10 ¹⁸	--

Table 1. Main parameters of the SC different layers^{16,21,28,33,37,38}.

Defect Parameters	Defect 1	Defect 2	Defect 3
Type	Single acceptor (-/0)	Single acceptor (-/0)	Single donor (0/+)
Distribution	Uniform	Uniform	Uniform
Electron/hole capture cross sections (cm ²)	1.0 × 10 ⁻¹⁵ / 1.5 × 10 ⁻¹⁷	1.0 × 10 ⁻¹⁵ / 4.9 × 10 ⁻¹³	4.0 × 10 ⁻¹³ / 1.0 × 10 ⁻¹⁵
Energy level (eV)	0.48 (above E _v)	0.71 (above E _v)	0.61 (below E _c)
Density (N _i) (cm ⁻³)	1.2 × 10 ¹⁵	1.1 × 10 ¹⁴	2.6 × 10 ¹⁴

Table 2. Bulk defect factors for the Sb₂(S, Se)₃ layer^{17,28,36,38}.

Interface Defect Parameters	ETL/Sb ₂ (S, Se) ₃
Type	Neutral
Electron/hole capture cross sections (cm ²)	1.0 × 10 ⁻¹⁵ /1.0 × 10 ⁻¹⁵
Distribution	Single
Trap level with respect to highest E _v (eV)	0.65
Density (cm ⁻²)	1 × 10 ¹⁵

Table 3. Interfacial defect parameters ETL/Sb₂(S, Se)₃ layers¹⁸.

ITO utilizing chemical bath deposition (CBD). Then, VTD was employed to obtain Sb₂(S, Se)₃ thin film over CdS. The deposition of Au on the absorber film was finally done by thermal evaporation³³.

An activation energy of recombination (E_a) was measured to be 0.97 eV according to¹⁶. The electron affinity of absorber (χ_{absorber}) is equal to 3.95 which fits the Sb₂S₃ mass ratio (ratio of S to S + Se) of 0.25¹⁷. Consequently, we can obtain a CBO value of -0.35 eV according to the relation³⁴.

$$E_a = E_{g,abs} - | \text{CBO} | \tag{1}$$

Where $E_{g,abs}$ is the absorber bandgap. Also, knowing that³⁵.

$$\text{CBO} = \Delta E_C = \chi_{\text{absorber}} - \chi_{\text{ETL}} \tag{2}$$

Then, the electron affinity of CdS (χ_{ETL}) is estimated to be 4.3 eV.

Table 2 shows Sb₂(S, Se)₃ bulk defect parameters with a high defect concentration of more than 1 × 10¹⁴ cm⁻³^{328,36}. The absorption coefficients are extracted from literature¹⁶. Further, the defect factors of Sb₂(S, Se)₃/CdS interface are selected to give acceptable fitting against measurements with surface recombination velocity (SRV) of 1 × 10⁷ cm/s, as given in Table 3. Finally, the parasitic series resistance (R_s) and the shallow uniform donor density N_D of CdS are supposed to be 2.3 Ω cm² and 2.9 × 10¹⁸ cm⁻³, respectively, to fit the experimental J - V curve.

Based on the parameters mentioned above, the simulated J - V curve is shown in Fig. 3(a), in comparison to the experimental curve¹⁷. The open-circuit voltage (V_{oc}), short-circuit current density (J_{sc}), fill factor (FF), and PCE recorded from simulation and experimental work³³ are listed in Table 4. This comparison indicates a decent agreement between experimental and simulated work. Alternatively, Fig. 3(b) presents the EBD, which is employed at short circuit and illumination conditions. E_c and E_v stand for the CB and VB edges, respectively. The EBD also shows how electrons move through the cliff from the absorber to the ETL. As can be seen from the EBD, the possibility of interfacial recombination at the ETL/absorber interface is high due to the low value of E_a (0.97 eV < $E_{g,abs}$). This suggests that a large portion of charge carriers may be lost due to non-radiative recombination processes. To mitigate these recombination losses and enhance charge extraction, careful band alignment engineering is essential to improve electron transfer efficiency.

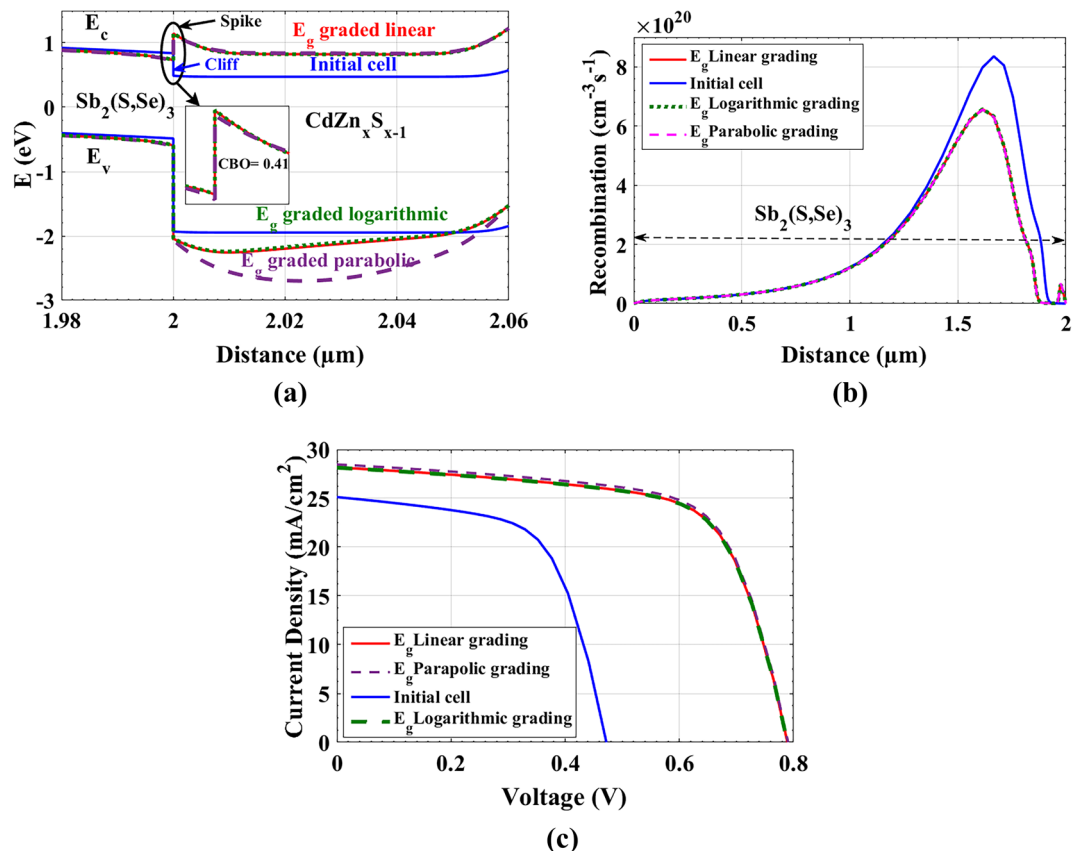


Fig. 3. Comparison between BGG of Cd_{1-x}Zn_xS (linear, logarithmic and parabolic) in illuminated HTL-free Sb₂(S, Se)₃ cells: (a) Energy bandgap bending in ETL and absorber illustrating the CBO on interface, (b) The recombination rate throughout the absorber, (c) *J*-*V* curves.

PV parameters	V _{oc} (V)	J _{sc} (mA/cm ²)	FF (%)	PCE (%)
Measurements	0.475	25.05	61.40	7.31
Calibration	0.474	25.12	61.41	7.31

Table 4. Comparison between measurements and calibration factors of the Sb₂(S, Se)₃ cell without HTL.

Result and discussion

The main purpose of employing suitable ETL and HTL is to accelerate the transition of electrons and holes from the absorber to the FC and back contact (BC), respectively, while inhibiting the movement of electrons and holes to the BC and FC as much as possible, respectively. Unfortunately, this produces electron and hole recombination at the ETL/absorber and HTL/absorber interfaces which lowers the SC performance. So, we utilize HTL-free design to minimize interface defects²⁷. In addition, we propose a grading technique in ETL to accomplish an identifiable band alignment between ETL and absorber in order to facilitate the stream of electrons from absorber to the FC. We choose Cd_{1-x}Zn_xS as ETL material which enables us to get different affinities and an appropriate CBO. Different grading profiles (linear, parabolic, and logarithmic) are investigated. To obtain more optimized SC, we study the effect of changing other technological parameters of the absorber. One of the most effective parameters is the acceptor doping. We examine the most suitable doping concentration and compare it with doping grading technique to get the most effective electric field in the absorber. In addition, we investigate the impact of varying thickness utilizing various percentages of the original bulk defects on the achieved PCE.

Bandgap grading profiles of Cd_{1-x}Zn_xS

Notably, the ternary compound Cd_{1-x}Zn_xS is a tunable bandgap material. It can be adjusted by varying the value of *x* to get the needed *E_g*. This feature makes Cd_{1-x}Zn_xS a promising candidate for the use as an ETL, replacing the single bandgap CdS. Its tunable bandgap enables appropriate band alignment throughout the cell from the front contact to the absorber. Figure S1 represents the variation of *χ* and *E_g* of Cd_{1-x}Zn_xS w.r.t. the composition *x* (see Supporting file).

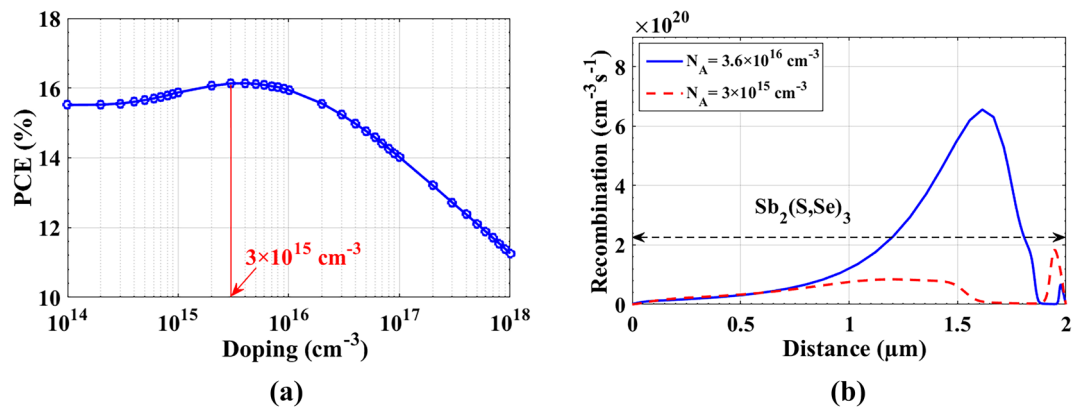


Fig. 4. (a) Change of PCE of HTL-free Sb₂(S, Se)₃ cells with absorber doping concentration, and (b) Comparison between recombination rates at zero bias across the absorber cell with $N_A = 3.6 \times 10^{16} \text{ cm}^{-3}$ and optimized doping cell with $N_A = 3 \times 10^{15} \text{ cm}^{-3}$.

PV parameters	V_{oc} (V)	J_{sc} (mA/cm ²)	FF (%)	PCE (%)
Linear BGG	0.7909	28.159	66.74	14.86
Logarithmic BGG	0.7908	28.134	66.73	14.85
Parabolic BGG	0.7921	28.567	66.84	15.07

Table 5. Illuminated parameters between BGG of CdZnS_{1-x} (linear, logarithmic and parabolic) of HTL-free Sb₂(S, Se)₃ structures.

To start, we began from $x=0.5$ at the right side to $x=0.81$ at the left side. This permits us to get the preferable CBO between ITO/ETL and ETL/Absorber. Beginning from ITO to 3.955 eV affinity of absorber passing through BGG of ETL with two different affinities at the two right and left interfaces is applied on the cell. This grading helps us to use different ETL electron affinities and bandgaps in the two sides (right side/FTO and left side/absorber) of material. We used BGG technique with different profiles (linear, logarithmic, and parabolic), which is simulated using SCAPS software, as shown in Figure S2 (see Supporting file). The three profiles are almost giving the same behavior in the CB, but it differs a lot in the VB, especially for parabolic profile as shown in Fig. 4(a). This technique presents a positive spike of 0.41 eV between ETL/absorber with three different profiles compared to the cliff in the initial calibrated cell. The cliff (CBO < 0) does not impede the carrier transport, yet the interface recombination is the main mechanism in the cell. On the other side, the spike happens if CBO > 0 and acts as a barrier for photo-generated electrons. However, the spike of 0.41 eV is low enough to permit electrons in CB to flow to front contact and holes in VB to flow to the BC which lowers the photo-generated carrier recombination at interfaces. This makes the SRH recombination is the major mechanism in this structure. Consequently, this excellent flow of carriers leads to a decrease in bulk recombination at absorber as shown in Fig. 4(b). Lowering bulk recombination appears strongly in an increase in J_{sc} . In addition, the mitigation of interface recombination leads to increasing V_{oc} , as displayed in Fig. 4(c). The optimized cell with parabolic BGG of ETL acquires the best profile behavior with the following metrics: $V_{oc} = 0.792 \text{ V}$, $J_{sc} = 28.57 \text{ mA/cm}^2$, FF = 66.84% and PCE = 15.07%, as illustrated in Table 5.

Figure 4. Comparison between BGG of Cd_{1-x}Zn_xS (linear, logarithmic and parabolic) in illuminated HTL-free Sb₂(S, Se)₃ cells: (a) Energy bandgap bending in ETL and absorber illustrating the CBO on interface, (b) The recombination rate throughout the absorber, (c) J - V curves.

Influence of the absorber doping concentration

Constant doping level optimization

Here, the acceptor doping level of the absorber was made to change from $N_A = 1 \times 10^{14} \text{ cm}^{-3}$ to $1 \times 10^{18} \text{ cm}^{-3}$ searching for enhancement of the performance of the cell. To obtain accurate results from this optimization, we used variable electron and hole mobility that is changing with every doping change as shown in Figure S3 (see Supporting file) following reference¹³. Figure 5(a) illustrates the change of the PCE versus absorber doping concentration. The optimum doping level is found to be $N_A = 3 \times 10^{15} \text{ cm}^{-3}$, which gives the following PV parameters: $V_{oc} = 0.743 \text{ V}$, $J_{sc} = 32.69 \text{ mA/cm}^2$, FF = 66.45% and PCE = 16.13%. The increase of PCE and J_{sc} is due to the effect of changing N_A to $3 \times 10^{15} \text{ cm}^{-3}$, which increases the carrier density of the absorber layer. However, excessively high doping concentrations can result in increased recombination rates due to carrier trapping effects as well as reduced carrier mobility. According to the easy photo-carrier transport from absorber, the bulk recombination is reduced, as established in Fig. 5(b).

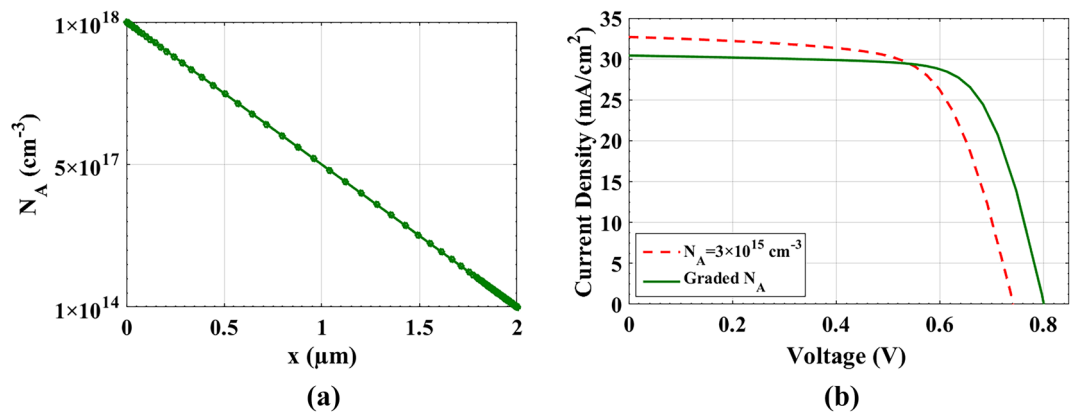


Fig. 5. (a) Grading doping concentration (N_A) along the absorber distance, and (b) comparison of J-V curves between optimized doping with $N_A = 3 \times 10^{15} \text{ cm}^{-3}$ and cell with graded N_A .

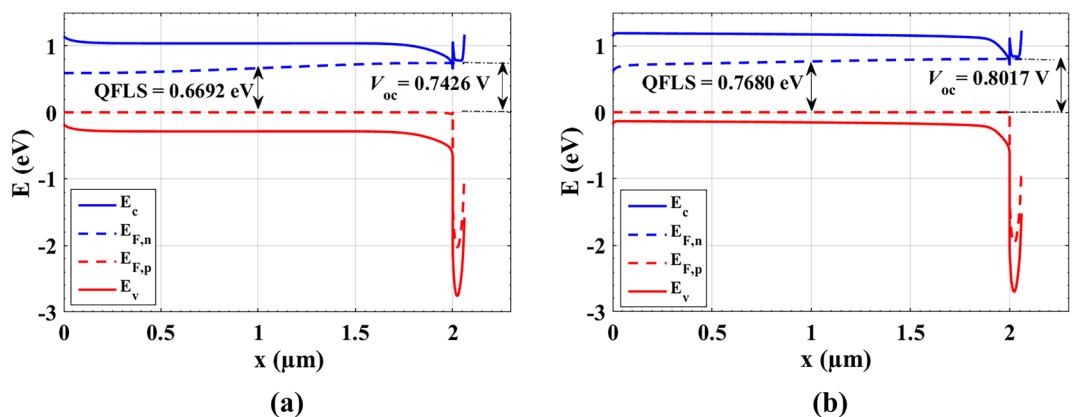


Fig. 6. Energy band diagram and Quasi Fermi level gradient at open circuit at absorber with (a) $N_A = 3 \times 10^{15} \text{ cm}^{-3}$ and (b) graded N_A .

PV parameters	V_{oc} (V)	J_{sc} (mA/cm^2)	FF (%)	PCE (%)
$N_A = 3 \times 10^{15} \text{ cm}^{-3}$	0.7426	32.692	66.45	16.13
Graded N_A	0.8017	30.420	72.36	17.65

Table 6. Illuminated parameters comparison between $N_A = 3 \times 10^{15} \text{ cm}^{-3}$ and N_A grading.

Doping grading

Here, we applied linear grading of doping starting with $N_A = 1 \times 10^{14} \text{ cm}^{-3}$ at the right side to $1 \times 10^{18} \text{ cm}^{-3}$ at the left side of absorber as shown in Fig. 6(a). Increasing doping at the BC acts as a back surface field that can improve the extraction of carriers thereby boost the V_{oc} . Figure 6(b) exhibits the J-V curves for two doping cases, namely, the linear grading doping technique and the fixed $N_A = 3 \times 10^{15} \text{ cm}^{-3}$ case. While the grading technique results in lowering the value of J_{sc} , other factors, FF and V_{oc} , are enhanced, resulting in a rise in the PCE. The reduction of the J_{sc} is mainly due to the reduced mobility resulting from higher doping levels.

The quantitative results, represented in Table 6, signify this conclusion. Figure 7 illustrates the energy band diagram (EBD) and Quasi Fermi level splitting (QFLS) at open-circuit conditions for two different absorber doping scenarios: (a) a uniformly doped absorber with $N_A = 3 \times 10^{15} \text{ cm}^{-3}$ and (b) a graded doping profile for N_A . In (a), the QFLS is 0.6692 eV , while in (b), it increases to 0.7680 eV , demonstrating that the graded doping enhances the separation of quasi-Fermi levels. Typically, a higher QFLS correlates with lower recombination rates and improved photovoltaic efficiency. This is clearly reflected in V_{oc} , where the simulated V_{oc} values are 0.7426 V for the uniform doping case (a) and 0.8017 V for the graded doping case (b). The increase in V_{oc} for the graded absorber suggests better carrier collection and lower non-radiative recombination, leading to an overall enhancement in device performance.

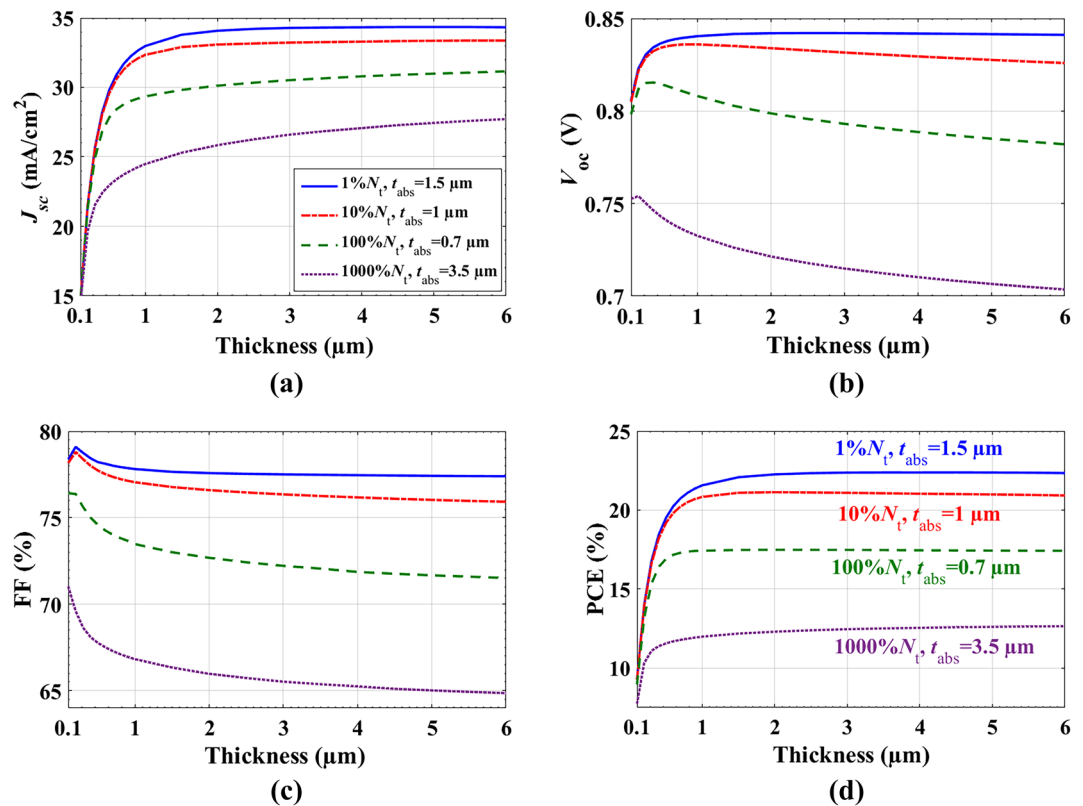


Fig. 7. PV parameters variation at different thicknesses and bulk defect densities of absorber (a) J_{sc} , (b) V_{oc} , (c) FF, and (d) PCE.

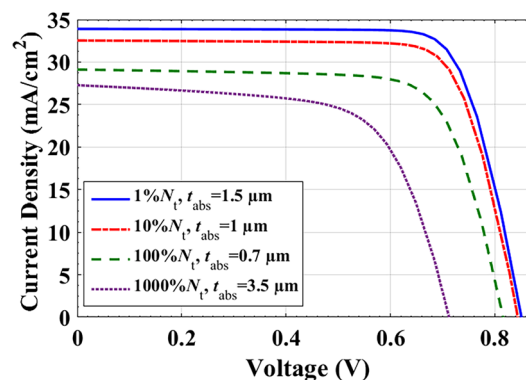


Fig. 8. J-V curves for different thicknesses and bulk defects of absorber.

Impact of absorber thickness and bulk defects

One of the key constraints that determines the PCE of a SC is the thickness of the absorber and the bulk trap density (N_t). To avoid more carrier recombination, it is preferable to use a thickness that is shorter than the carrier's diffusion length. However, higher absorption of sunlight necessitates a sufficiently large thickness. In addition, electron and hole recombination depends significantly on N_t . Thus, examining the effect of absorber thickness in relation to total bulk traps is essential to achieving high PCE.

In these simulations, the absorber thickness is adjusted to be from 0.1 to 6 μm . Figure 8 shows the PV behavior of the cell at different bulk density percentages 1%, 10%, 100%, 1000% of the value used in calibration, N_t . The contour plots for these changes are shown in Figure S4. For each value of N_t , there is a certain absorber thickness at which the cell shows maximum efficiency. Figure 8(d) presents the best suggested t_{abs} (μm) and N_t (cm^{-3}) for each case. Based on these choices, we plotted the J-V characteristics of four cells, as demonstrated in Fig. 9. The corresponding PV parameters are listed in Table 7. As seen, there is no extreme change in the PV parameters between cell 1 and cell 2. Therefore, the optimum PCE can be selected for cell 2 with the optimized

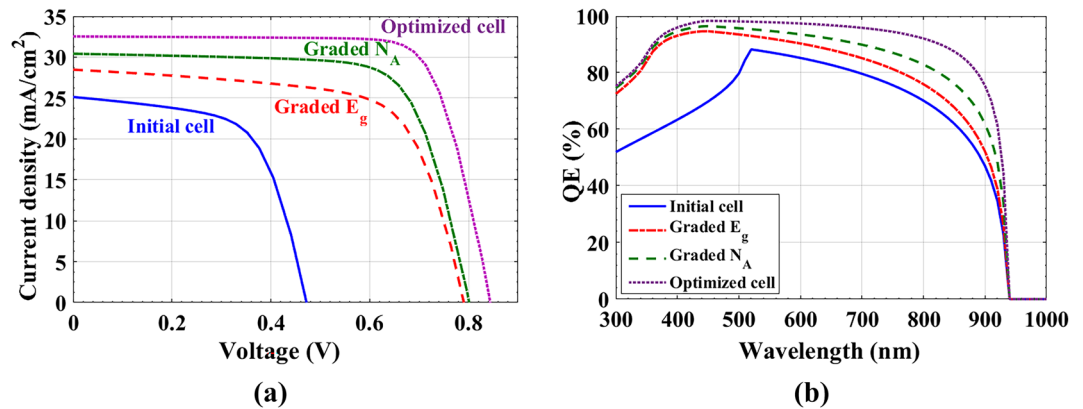


Fig. 9. J-V for different optimization cases of the HTL free SC: (a) J-V curves. (b) quantum efficiency.

PV parameters	V_{oc} (V)	J_{sc} (mA/cm ²)	FF (%)	PCE (%)
Cell 1 (1% N_t , $t_{abs}=1.5$ μ m)	0.85	33.90	77.46	22.41
Cell 2 (10% N_t , $t_{abs}=1$ μ m)	0.85	32.54	76.88	21.15
Cell 3 (100% N_t , $t_{abs}=0.7$ μ m)	0.82	29.12	73.63	17.52
Cell 4 (1000% N_t , $t_{abs}=3.5$ μ m)	0.71	27.27	65.23	12.69

Table 7. PV factors of the simulated cell for different cases of thickness and bulk defects.

parameters (10% N_t , $t_{abs} = 1$ μ m), which supports low-cost SC with acceptable total bulk defects and small thickness. The optimized metrics of cell 2 are: $V_{oc} = 0.85$ V, $J_{sc} = 32.54$ mA/cm², FF = 76.88%, and PCE = 21.15%.

Final optimization

All the above are trails to get more efficient solar cells with more photo-absorption and less bulk and interface recombination. The resulted optimized cell has absorber with physical parameters: $t_{abs} = 1$ μ m, bulk defects has been decreased to 10% N_t cm⁻³, linear doping grading, and parabolic BGG of Cd_{1-x}Zn_xS as ETL. Figure 10(a) illustrates the J-V curves, and the improvement attained for J_{sc} and V_{oc} during the last steps with comparison to the initial cell. Table 8 presents a PV parameters' comparison between all the previous optimized steps. Figure 10(b) shows the simulated external quantum efficiency (EQE) versus wavelength. As shown, the sunlight absorption of the initial cell is very weak in the 300–500 nm range. The optimized steps achieve significant progress in absorption, especially in the UV range.

Energy loss analysis

To assess energy losses in the analyzed cells, we separate the different energy losses following references^{39,40}. The energy losses can be divided into (where $\Phi(h\nu)$ is the solar energy spectrum and $h\nu$ is the photon energy):

- Transmission loss: $E_{trans} = \int_0^{E_g} \Phi(h\nu) d h\nu$
- Insufficient light-absorbing: $E_{abs} + E_{IQE} = \int_{E_g}^{4.43} (1 - EQE(h\nu)) \Phi(h\nu) d h\nu$
- Thermalization energy loss: $E_{th} = \int_{E_g}^{4.43} \left(1 - \frac{E_g}{h\nu}\right) EQE(h\nu) \Phi(h\nu) d h\nu$
- Open circuit voltage (V_{oc}) loss: $E_{V_{oc}} = \int_{E_g}^{4.43} \left[\frac{E_g - V_{oc}}{h\nu}\right] EQE(h\nu) \Phi(h\nu) d h\nu$
- Filling Factor (FF) loss: $E_{FF} = (1 - FF) \left(\int_{E_g}^{4.43} \Phi(h\nu) d h\nu - E_{trans} - E_{abs} - E_{IQE} - E_{therm} - E_{V_{oc}} \right)$

Figure 10 shows the energy loss components, while Table 9 compares all the distributed energy components of both initial and optimized SCs. In the optimized case, the absorption energy loss (E_{abs}) has been significantly reduced from 18.316 W/cm² (initial value) to 4.358 W/cm². Notably, optimizing the absorber thickness and doping concentration reduces absorption loss by increasing the light absorption in the Sb₂(S, Se)₃ layer. On the other hand, there is an increase in thermal energy loss (E_{th}) in the optimized structure, rising from 18.032 to 22.84 W/cm². However, since the number of photons absorbed can impact the thermalization loss, we define the thermalization loss per electron ($E_{therm}/N_{electrons}$) as a more reasonable comparing metric. The average thermalization loss per electron in initial and optimized cells is found to be 0.719, and 0.701 eV, respectively. Thus, although the total thermalization loss is increased in the optimized cell due to the increased light absorption

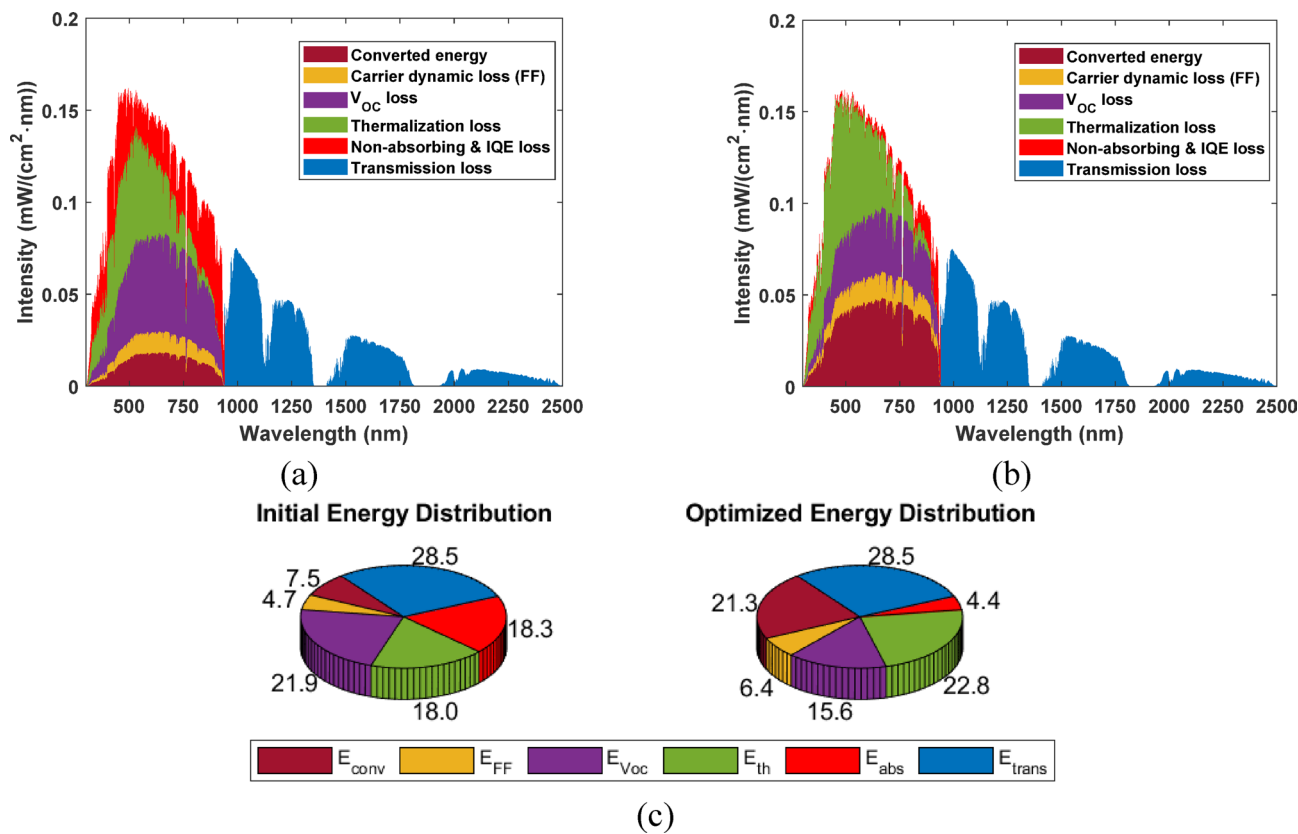


Fig. 10. Spectral power density distribution shows the energy loss components in (a) the initial cell structure and (b) the optimized cell structure, while the integrated power loss is given for the two structures in (c).

PV parameters	V _{oc} (V)	J _{sc} (mA/cm ²)	FF (%)	PCE (%)
Measurements	0.475	25.05	61.4	7.31
Initial cell	0.474	25.12	61.41	7.31
Grad (ETL) E _g parabolic	0.792	28.56	66.84	15.07
Grad (Absorber) doping	0.801	30.42	72.36	17.65
Thickness & defects optimization	0.845	32.54	76.88	21.15

Table 8. PV parameters’ comparison between all the previous optimized steps.

W/cm ²	E _{trans}	E _{abs}	E _{th}	E _{VOC}	E _{FF}	E _{conv}
Initial	28.526	18.316	18.032	21.858	4.726	7.521
Optimized	28.526	4.358	22.84	15.565	6.402	21.287

Table 9. Comparison between the distributed energy components of initial and optimized cells.

(as evident from the EQE in Fig. 10(b)), the thermalization energy loss per electron is reduced by distributing the light intensity among electrons.

Regarding open-circuit voltage energy loss (E_{VOC}), E_{VOC} has decreased from 21.858 to 15.565 W/cm², which is attributed to the optimized doping profile and reduced recombination. The fill-factor energy loss E_{FF} has increased in the optimized configuration from 4.726 to 6.402 W/cm². Overall, the converted energy is shown to have a significant increase in the optimized configuration, from 7.5206 to 21.287 W/cm², indicating a significantly higher overall energy conversion efficiency.

Finally, Table 10 shows a comparison between some HTL-free Sb₂(S, Se)₃ structures that have been studied experimentally and theoretically over the last few years. This comparison illustrates the gradual progress made in research towards achieving a highly efficient solar cell with low cost, safe and easy fabrication. There are a lot of HTL-free cells that use different ETLs. Starting with H. Deng and his team in 2018, they made

Reference	ETL	Approach	PCE (%)
29	TiO ₂	Experimental	5.6%
33	CdS	Experimental	7.31
9	CdS	Experimental	6.30
41	ZnO/CdS	Experimental	5.73%
18	Cd _{0.44} Zn _{0.56} S	Simulation	14.86%
27	Cd _{0.44} Zn _{0.56} S	Simulation	21.86.
2	Zn _{0.85} Mg _{0.15} O	Simulation	20
This work	CdS	Simulation	7.31
This work	E _g Graded Cd _{1-x} Zn _x S	Simulation	15.07
This work	E _g Graded Cd _{1-x} Zn _x S, N _A = 3 × 10 ¹⁵ cm ⁻³	Simulation	16.13
This work	E _g Graded Cd _{1-x} Zn _x S, Graded N _A	Simulation	17.65
This work	E _g Graded Cd _{1-x} Zn _x S, Graded N _A , 10% N _t , t _{abs} = 1 μm	Simulation	21.15

Table 10. A state-of-the-art quantitative comparison between Sb₂(S, Se)₃ cells without HTL performed by experimental and simulated studies.

significant experimental progress from 1.8 to 5.6% PCE by using Sb₂(Se_{0.68}S_{0.32})₃ as an absorber and TiO₂ as an ETL. Furthermore, Ishaq et al. 2018 experimentally introduced double buffer layer ZnO/CdS for the first time in the Sb₂(Se_{0.68}S_{0.32})₃ system which improves efficiency from 4.17 to 5.73%. In 2021, Xiaobo Hu et al., fabricated Sb₂(S_{0.25}, Se_{0.75})₃ thin films using the VTD method and got 7.31% PCE. For the band alignment at the ETL/absorber interface, others used different ETLs to modify the CBO. M. S. Salem et al., in 2022, utilized Zn_{0.85}Mg_{0.15}O in HTL-free SC and achieved 20% PCE.

Conclusions

In this paper, we introduced single junction SC based on Sb₂(S, Se)₃ as an absorber. The cell is designed as HTL-free for low cost and more stability. The applied cell is simulated by the numerical simulator SCAPS-1D. The Simulation parameters are adjusted to satisfy good agreement comparable to the experimental data. The simulated cell performance is investigated under various effects such as CBO adjustment between ETL and absorber, absorber doping concentration, absorber thickness and bulk trap defects. It was concluded that CBO is the most effective parameter. To get more effective CBO for this cell, we replaced the CdS with the tunable bandgap CdZnS composite. Optimizing CBO is applied by ETL parabolic grading technique. Choosing two different compositions of Zn (0.5, 0.81) at the two interfaces enables to grade the electron affinity from absorber to front contact. This ETL grading improved performance drastically (more than 100%) relative to the initially simulated cell. The optimized cell parameters satisfy $V_{oc} = 0.792$ V, $J_{sc} = 28.56$ mA/cm², FF = 66.84% and PCE = 15.07%. Furthermore, the acceptor doping is optimized by grading it across the absorber from 1×10^{15} to 1×10^{18} cm⁻³. This step raises the PCE to 17.65% due to the increase in the difference between electron and hole fermi levels despite increasing the J_{sc} . More over, the influence of thickness and trap defects of the absorber are also investigated. Reducing the thickness to one half ($t_{abs} = 1$ μm) with bulk defects of 10% of the initial defects result in the following PV parameters: $V_{oc} = 0.845$ V, $J_{sc} = 32.54$ mA/cm², FF = 76.88%, and PCE = 21.15%.

This study promotes the usage of the HTL-free Sb₂(S, Se)₃ SC design and points to various techniques for the optimization of solar cell performance by grading numerous parameters to control the flow of electrons between the layers and to achieve higher efficiency along with predicted low-cost and higher stability.

Data availability

All data that support the findings of this study are included within the article (and any supplementary files).

Received: 12 May 2025; Accepted: 11 July 2025

Published online: 25 July 2025

References

- Abdelkadir, A. A. et al. New Sb₂Se₃ based solar cell for achieving high efficiency-Theoretical modeling. *Opt. Quant. Electron.* **55** (6), 514 (2023).
- Salem, M. S. et al. Numerical analysis of hole transport layer-free antimony Selenide solar cells: possible routes for efficiency promotion. *Opt. Mater.* **129** (1), 112473 (2022).
- Green, M. A. et al. Solar cell efficiency tables (version 66). *Prog. Photovoltaics Res. Appl.* **33**, 795–810 (2025).
- Salem, M. S. et al. Performance investigation of a proposed flipped npn microstructure silicon solar cell using TCAD simulation. *Crystals* **12**(7), 959 (2022).
- Carron, R. et al. Advanced alkali treatments for high-efficiency Cu(In,Ga)Se₂ solar cells on flexible substrates. *Adv. Energy Mater.* **9**(24), 1900408 (2019).
- Nakamura, M. et al. Cd-Free Cu (In,Ga)(Se,S)₂ Thin-Film solar cell with record efficiency of 23.35%. *IEEE J. Photovolt.* **9** (6), 1863–1867 (2019).
- Ramanujam, J. et al. Flexible CIGS, CdTe and a-Si:H based thin film solar cells: A review. *Prog Mater. Sci.* **110**, 100619–100638 (2020).
- Kondrotas, R., Chen, C. & Tang, J. Sb₂S₃ solar cells. *Joule* **2**(5), 857–878 (2018).

9. Lu, S. et al. $\text{Sb}_2(\text{Se}_{1-x}\text{S}_x)_3$ Thin-Film solar cells fabricated by Single-Source vapor transport deposition. *Solar RRL*. **3** (4), 1800280 (2019).
10. Parekh, Z. R. et al. Growth of a CuSbSe_2 single crystal by the Bridgman technique and its utility as a photodetector and thermoelectric material. *Mater. Adv.* **5**, 4832–4847 (2024).
11. Zhang, Y., Huang, J. & Cong, J. Cu_{Sb} : The dominant defect in Cu-rich CuSbS_2 solar cells fabricated by sulfurizing co-sputtered Cu–Sb precursor. *Sol. Energy Mater. Sol. Cells*. **273**, 112935 (2024).
12. Shen, K. et al. Efficient and stable planar n–i–p Sb_2Se_3 solar cells enabled by oriented 1D trigonal selenium structures. *Adv. Sci.* **7** (16), 2001013 (2020).
13. Liang, G. et al. Ion doping simultaneously increased the carrier density and modified the conduction type of Sb_2Se_3 thin films towards quasi-homojunction solar cell. *J. Materiomics*. **7** (6), 1324–1334 (2021).
14. Li, Z. et al. 9.2%-efficient core-shell structured antimony Selenide Nanorod array solar cells. *Nat. Commun.* **10** (1), 125 (2019).
15. Dong, J. et al. Carrier management through electrode and electron-selective layer engineering for 10.70% efficiency antimony selenosulfide solar cells, Nature energy (2025).
16. Tang, R. et al. Hydrothermal deposition of antimony Selenosulfide thin films enables solar cells with 10% efficiency. *Nat. Energy*. **5** (8), 587–595 (2020).
17. Li, K. et al. Over 7% efficiency of $\text{Sb}_2(\text{S,Se})_3$ solar cells via v-shaped bandgap engineering. *Solar RRL*. **4**(9), 2000220 (2020).
18. Salem, M. S., Shaker, A., Almurayziq, T. S. & Alshammari, M. T. Prospective efficiency boosting of full-inorganic single-junction $\text{Sb}_2(\text{S,Se})_3$ solar cell. *Sol. Energy Mater. Sol. Cells*. **248** (2), 112001 (2022).
19. Lu, S. et al. Sb_2Se_3 thin-film photovoltaics using aqueous solution sprayed SnO_2 as the buffer layer. *Adv. Electron. Mater.* **4**(1), 1700329 (2018).
20. Li, G. et al. Improvement in Sb_2Se_3 solar cell efficiency through band alignment engineering at the buffer/absorber interface. *ACS Appl. Mater. Interfaces*. **11** (1), 828–834 (2019).
21. Cao, Y. et al. Theoretical insight into high-efficiency triple-junction tandem solar cells via the band engineering of antimony chalcogenides. *Solar RRL*. **5**(4), 2000800 (2021).
22. Chen, J. et al. Se-Elemental concentration gradient regulation for efficient $\text{Sb}_2(\text{S,Se})_3$ solar cells with high Open-Circuit voltages. *Angew. Chem.* **63** (40), e202409609 (2024).
23. Huang, L. et al. Temperature-Gradient solution deposition amends unfavorable band structure of $\text{Sb}_2(\text{S,Se})_3$ film for highly efficient solar cells. *Angew. Chem. Int. Ed.* **63** (26), e202406512 (2024).
24. Zhang, J. et al. Over 10% efficient $\text{Sb}_2(\text{S,Se})_3$ solar cells enabled by CsI -doping strategy. *Small* **20** (27), 2310418 (2024).
25. Deng, Y. et al. Carbon-Based $\text{Sb}_2(\text{S,Se})_3$ Solar Cells. *Inorganics (Basel)*. **11** (4), 159 (2023).
26. Chen, W. et al. Superior intermolecular noncovalent interactions empowered dopant-free hole transport materials for efficient and stable $\text{Sb}_2(\text{S,Se})_3$ solar cells. *Adv. Funct. Mater.* **34** (22), 2313403 (2024).
27. Salem, M. S. et al. Numerical analysis and design of high performance HTL-free antimony sulfide solar cells by SCAPS-1D. *Opt. Mater.* **123** (2), 111880 (2022).
28. Lu, Y. et al. HTL-Free $\text{Sb}_2(\text{S,Se})_3$ Solar Cells with an Optimal Detailed Balance Band Gap. *ACS Appl. Mater. Interfaces*. **13** (39), 46858–46865 (2021).
29. H.Deng, S. et al. High-throughput method to deposit continuous composition spread $\text{Sb}_2(\text{Se}_x\text{S}_{1-x})_3$ thin film for photovoltaic application. *Prog. Photovoltaics Res. Appl.* **26** (4), 281–290 (2018).
30. Kowsar, A. et al. Comparative Study on Solar Cell Simulators, 2nd International Conference on Innovation in Engineering and Technology (2019).
31. Yao, H. & Liu, L. Design and optimize the performance of self-powered photodetector based on PbS/TiS_3 heterostructure by SCAPS-1D. *Nanomaterials* **12** (3), 325 (2022).
32. Qaid, S. M. H. et al. Optoelectronic device modeling and simulation of Selenium-Based solar cells under LED illumination. *Crystals* **13** (12), 1668 (2023).
33. Hu, X. et al. Fabricating over 7%-efficient $\text{Sb}_2(\text{S,Se})_3$ thin-film solar cells by vapor transport deposition using Sb_2Se_3 and Sb_2S_3 mixed powders as the evaporation source. *J. Power Sources*. **493** (1), 229737 (2021).
34. Das, A. et al. A simulation investigation of lead-free inorganic CsGeI_3 -based perovskite for solar cell with hole transport layers of different organic materials via SCAPS-1D modeling. In *Nanomaterials for Sensors and Sustainable Energy*. Materials Horizons: From Nature to Nanomaterials, Vol. 1 (eds Ameen, S., Akhtar, M.S. & Kong, I.) (Springer, Singapore, 2025). https://doi.org/10.1007/978-981-96-0660-3_6
35. Saadat, M. & Bameri, S. Comprehensive analysis of transport layers and interface defects in MAPbI_3 based PSCs for enhanced efficiency. *Discover Appl. Sci.* **7**, 440 (2025).
36. Wen, X. et al. Vapor transport deposition of antimony Selenide thin film solar cells with 7.6% efficiency. *Nat. Commun.* **9** (1), p2179 (2018).
37. Kartopu, G. et al. Effect of window layer composition in $\text{Cd}_{1-x}\text{ZnxS}/\text{CdTe}$ solar cells. *Prog. Photovoltaics Res. Appl.* **22** (1), 18–23 (2014).
38. Chen, C. et al. 6.5% certified Sb_2Se_3 solar cells using PbS colloidal quantum Dot film as hole transporting layer. *ACS Energy Lett.* **2** (9), 2125–2132 (2017).
39. Zuo, L. et al. Tackling energy loss for High-Efficiency organic solar cells with integrated multiple strategies. *Adv. Mater.* **30** (16), 1706816 (2018).
40. Wu, X. et al. Improved stability and efficiency of perovskite/organic tandem solar cells with an all-inorganic perovskite layer. *J. Mater. Chem. A*. **9** (35), 19778–19787 (2021).
41. Ishaq, M. et al. Efficient double buffer layer $\text{Sb}_2(\text{Se}_x\text{S}_{1-x})_3$ thin film solar cell via single source evaporation. *Solar RRL*. **2** (10), 1800144 (2018).

Author contributions

Basma A. A. Osman: Conceptualization, Methodology, Software, Validation, Formal analysis, Investigation, Data curation, Writing—original draft, Writing—review and editing; Ahmed Shaker: Methodology, Validation, Formal analysis, Software, Supervision, Writing—review and editing; Ibrahim S. Ahmed: Methodology, Formal analysis, Investigation, Writing—original draft, Writing—review and editing; Tarek M. Abdolkader: Conceptualization, Formal analysis, Investigation, Validation, Supervision, Writing—original draft.

Funding

Open access funding provided by The Science, Technology & Innovation Funding Authority (STDF) in cooperation with The Egyptian Knowledge Bank (EKB).

Declarations

Competing interests

The authors declare no competing interests.

Additional information

Supplementary Information The online version contains supplementary material available at <https://doi.org/10.1038/s41598-025-11658-8>.

Correspondence and requests for materials should be addressed to A.S.

Reprints and permissions information is available at www.nature.com/reprints.

Publisher's note Springer Nature remains neutral with regard to jurisdictional claims in published maps and institutional affiliations.

Open Access This article is licensed under a Creative Commons Attribution 4.0 International License, which permits use, sharing, adaptation, distribution and reproduction in any medium or format, as long as you give appropriate credit to the original author(s) and the source, provide a link to the Creative Commons licence, and indicate if changes were made. The images or other third party material in this article are included in the article's Creative Commons licence, unless indicated otherwise in a credit line to the material. If material is not included in the article's Creative Commons licence and your intended use is not permitted by statutory regulation or exceeds the permitted use, you will need to obtain permission directly from the copyright holder. To view a copy of this licence, visit <http://creativecommons.org/licenses/by/4.0/>.

© The Author(s) 2025